Distinct Impact of Alkali-Ion Doping on Electrical Transport Properties of Thermoelectric *p*-Type Polycrystalline SnSe

Tian-Ran Wei,[†,‖] Gangjian Tan,[‡,‖] Xiaomi Zhang,[§] Chao-Feng Wu,[†] Jing-Feng Li,*[,†] Vinayak P. Dravid,[§] G. Jeffrey Snyder,[§] and Mercouri G. Kanatzidis[‡]

[†]State Key Laboratory of New Ceramics and Fine Processing, School of Materials Science and Engineering, Tsinghua University, Beijing 100084, China

[‡]Department of Chemistry, Northwestern University, Evanston, Illinois 60208, United States

[§]Department of Materials Science and Engineering, Northwestern University, Evanston, Illinois 60208, United States

S *Supporting Information*

ABSTRACT: Recent findings about ultrahigh thermoelectric performance in SnSe single crystals have stimulated related research on this simple binary compound, which is focused mostly on its polycrystalline counterparts, and particularly on electrical property enhancement by effective doping. This work systematically investigated the thermoelectric properties of polycrystalline SnSe doped with three alkali metals (Li, Na, and K). It is found that Na has the best doping efficiency, leading to an increase in hole concentration from 3.2×10^{17} to 4.4×10^{19} cm^{-3} at room temperature, accompanied by a drop in Seebeck coefficient from 480 to 142 μV/K. An equivalent single parabolic band model was found adequate to capture the variation tendency of Seebeck coefficient with doping levels within a wide range. A mixed scattering of carriers by acoustic phonons and grain boundaries is suitable for numerically understanding the temperature-dependence of carrier mobility. A maximum *ZT* of ~0.8 was achieved in 1% Na- or K-doped SnSe at 800 K. Possible strategies to improve the mobility and *ZT* of polycrystals were also proposed.
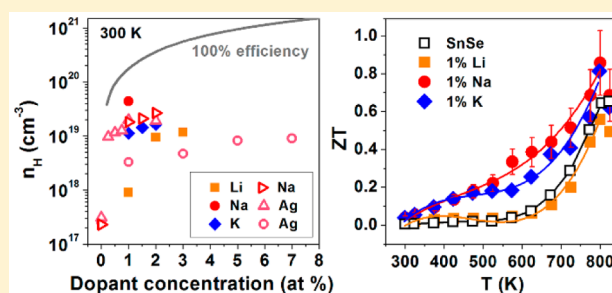
INTRODUCTION

The worldwide demand for reduced dependence on carbon-based fuels and the increasing interest in cutting energy waste have made thermoelectrics one of the most fascinating topics in the field of sustainable energy utilization.[1,2] The efficiency of thermoelectric conversion is mostly dependent on the materials' dimensionless figure of merit, $ZT = S^2T/\rho\kappa$, where S, T, ρ, and κ are Seebeck coefficient, absolute temperature, electrical resistivity, and thermal conductivity, respectively.[3] Scientific progress has been significant in the past two decades in exploring high-performance thermoelectric materials,[4,5] and *ZT* records have been renewed in several state-of-the-art thermoelectric systems, such as lead chalcogenides[6−8] and Bi$_2$Te$_3$-based compounds.[9,10]

At the same time, however, the search has never ceased for new, high-performance materials composed of Earth-abundant, inexpensive, and low-toxicity elements.[11−13] Recently, the binary compound SnSe has been discovered to exhibit an ultrahigh thermoelectric performance in both undoped and *p*-type doped single crystals.[14−16] The compound benefits from both the multi-valley feature of its valence bands[15] and a very low thermal conductivity.[17] Meanwhile, growing attention has also been paid to its polycrystalline counterparts considering their better machinability.[18,19] Relatively high *ZT* values ranging from 0.6 to 1.1 (at 773−823 K) have been achieved in

polycrystalline samples via doping,[20] alloying,[21,22] and micro-structure modulation,[23,24] but their performance is still considerably inferior to that of single crystals. Because the growth of single crystals is challenging due to a strong phase transition at high temperature and the performance is high only along the crystallographic *bc*-plane, the ultimate goal is to enhance *ZT* of polycrystalline samples. This can be realized through a deep understanding of the electrical and thermal transport properties and exquisite control of the crystallite orientation in the samples.

Chemical doping has been widely adopted to tune the carrier concentration and improve the *ZT* of thermoelectric materials.[25,26] For SnSe, Ag[19,27] and Na[20,22,28] were used as *p*-type dopants, while I[18] and BiCl$_3$[29] were *n*-type ones. However, a deep understanding of non-stoichiometry, electronic band structure and the scattering process in polycrystalline SnSe is scarce so far, and more studies are needed in order to develop a useful guide to optimize the thermoelectric properties.

In this work we chose Li, Na, and K as *p*-type dopants to optimize the carrier concentration and enhance *ZT* of polycrystalline SnSe. All the three alkali-metal dopants
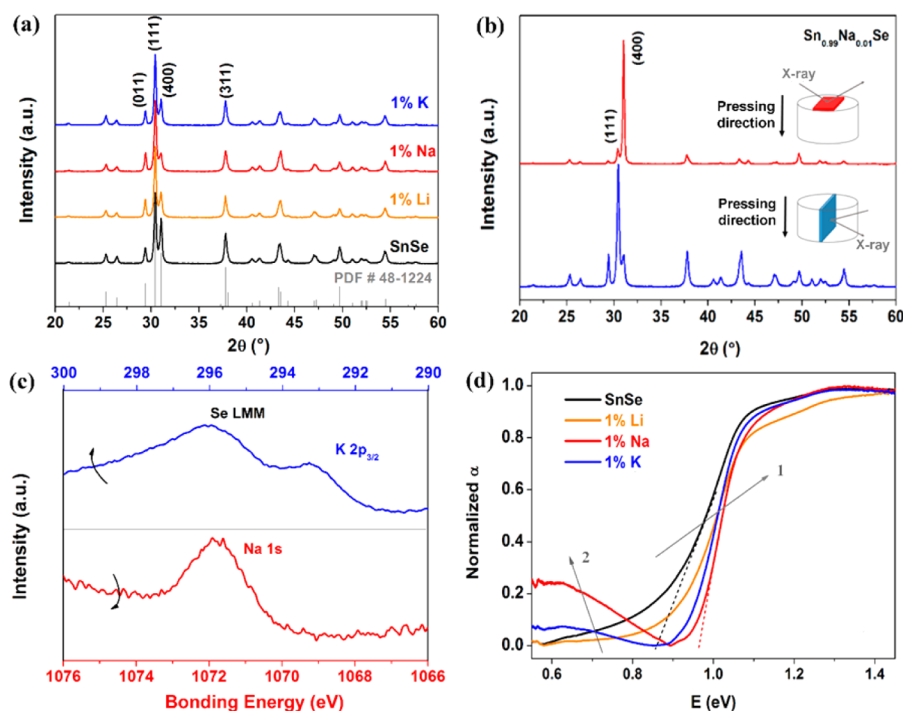
Figure 1. XRD patterns of (a) SnSe-based materials and (b) a Na-doped sample along two different directions; obvious difference in the relative peak intensity of (400) and (111) is seen, indicating strong anisotropy of the bulk samples. (c) High-resolution XPS spectra of Na (1s) and K ($2p_{3/2}$); one or a series of Se LMM Auger electron bonding energy peak(s) was (were) detected near the K $2p_{3/2}$ signal. (d) Optical absorption spectra for SnSe-based materials; arrow 1 in shows the Burstein−Moss shift and arrow 2 indicates enhanced free-carrier absorption.

increased the carrier concentration, and particularly, Na showed the best doping efficiency while maintaining a relatively high Seebeck coefficient. An equivalent single parabolic band with an effective mass of ∼1.0 m_0 (m_0 is the mass of a free electron) can reasonably describe the dependence of Seebeck coefficient on doping level over a wide range. The dependence of mobility on temperature was numerically analyzed considering a mixed scattering of carriers by acoustic phonons and energy barriers at grain boundaries. A maximum ZT of ∼0.8 at 800 K was achieved in 1% Na- and K-doped samples, which is ∼30% higher than that of undoped SnSe.

■ EXPERIMENTAL SECTION

Synthesis. Polycrystalline SnSe samples were synthesized by the conventional melting, annealing method. Stoichiometric Sn chunks (99.999%, American Elements, US), Se granules (99.999%, 5N Plus, Canada), and the alkali metal pieces (99.9%, Sigma-Aldrich, US) were weighed and loaded into a 10 mm diameter quartz tube. For a typical experiment to prepare 10 g of $Sn_{0.99}Na_{0.01}Se$, Sn (5.9744 g), Se (4.0140 g), and Na (0.0117 g) were used. For Li-, Na-, and K-doping cases, the inner wall of the tube was coated with carbon to prevent possible reaction between the alkali metals and the wall. The tube was evacuated to 10^{-4} Torr, flame-sealed, and then put into a larger 13 mm diameter quartz tube that was again evacuated and sealed. The outer tube was used to protect the material from oxidation because the inner tube always breaks when cooling down owing to the difference in lattice constants between high- and low-temperature phases. The double-tube was vertically placed in a box furnace, slowly heated to 1223 K in 10 h, held for 8 h and slowly cooled to 873 K over 4 h, and kept at that temperature for 2 days followed by a furnace cooling to room temperature. The obtained ingots were cleaned and pulverized into fine powders by hand, which were subsequently densified by spark plasma sintering (SPS, SPS-211LX, Fuji Electronic Industrial Co., Ltd., Japan) at 873 K for 5 min, producing a cylinder-shaped sample of ∼12.7 mm in diameter and ∼8 mm in height.

Characterization. Samples' phase purity was studied using X-ray diffraction (XRD, RINT 2000, Rigaku, Japan) with Cu Kα radiation. The elemental composition of the bulk samples was further studied by X-ray photoelectron spectroscopy (XPS, Escalab 250Xi; Thermo Scientific, UK) with Al Kα radiation. Optical absorption spectra of powders were collected using the UV−vis−NIR spectrum system (Cary 5000, Varian, USA). Fractured and polished surfaces of the bulk samples were examined by the field emission scanning electron microscopy (FE-SEM, JSM-7001, JEOL, Japan) in both secondary electron (SE) and backscattered electron (BSE) modes. A scanning/transmission electron microscopy (S/TEM) investigation was conducted using JEOL 2100F microscope operated at 200 kV. Energy-dispersive X-ray spectroscopy (EDS) equipped on FE-SEM and S/TEM, and electronic probe microscopic analysis (EPMA, JXA-8230, JEOL, Japan) with wavelength-dispersive spectrometer (WDS), were employed to investigate the actual ratio and the elemental distribution. Contents of alkali elements in doped samples were analyzed by inductively coupled plasma optical emission spectroscopy (ICP-OES, VISTA-MPX, Varian, USA).

Transport Property Measurement. Seebeck coefficient (S) and electrical resistivity (ρ) of bar-shaped samples were measured using a Seebeck coefficient/electric resistance measuring system (ZEM-3, Ulvac-Riko, Japan). Temperature-dependent Hall coefficient (R_H) was measured by the Van der Pauw technique using a commercial system (ResiTest 8340DC, Toyo, Japan). Hall carrier concentration (n_H) and mobility (μ_H) were calculated via $n_H = 1/(eR_H)$ and $\mu_H = R_H/\rho$, respectively. Thermal diffusivity (D) was measured on a square specimen of ∼6 mm in length and ∼2 mm in thickness by using a laser flash method (LFA457, Netsch, Germany). The specific heat capacity (C_P) was taken from refs 14 and 15. Thermal conductivity (κ) was calculated by $\kappa = DC_Pd$, in which d is the density calibrated using the Archimedes method. Due to the layered structure of SnSe, both the electrical and thermal transport properties of all the samples were measured perpendicular to the SPS pressure direction (i.e., in-plane measurements).

RESULTS AND DISCUSSION

Phase, Dopability, and Microstructure. XRD patterns of both undoped and doped SnSe polycrystalline SPSed samples are shown in Figure 1a. All the peaks were indexed to the orthorhombic phase with a *Pnma* symmetry. No second phase was observed within the detection limit of the X-ray. Structural anisotropy is clearly indicated in the XRD patterns performed on specimen cut along different directions (Figure 1b) because of its layered crystal structure. The presence of the dopants was reflected by XPS spectra in which Na 1s and K $2p_{3/2}$ peaks were detected around 1072 and 293 eV, respectively (Figure 1c), while the Li 1s peak is mostly overlapped by the strong Se 3d signals, which share similar bonding energies of 54−56 eV.

The doping evidence was further confirmed by the difference in the optical absorption spectra. As shown in Figure 1d, undoped SnSe exhibits an absorption edge around 0.85 eV that is in agreement with the reported band gap (E_g).[14,22] When doped with alkali ions, a distinct blue-shift is seen to 0.89, 0.93, and 0.96 eV for Li-, K-, and Na-doping cases, respectively (arrow 1), indicating the widening of the apparent, optical band gap, E_{opt}. This phenomenon is ascribed to the Burstein−Moss effect.[30,31] According to this effect, the Fermi level of a degenerate *p*-type semiconductor lies in the valence band, and thus a carrier from the highest occupied level needs more energy to be excited to the conduction band edge. Therefore, the so-called Burstein−Moss shift is a measure of the doping level; the larger it is, the deeper Fermi level lies, suggesting a higher carrier concentration. In addition, an increase of absorption at lower energies with doping (especially with Na or K, arrow 2) was observed due to the enhanced free-carrier contribution,[32,33] again indicating increased carrier concentration with Na- and K-doping.

SnSe-based polycrystals ($Sn_{0.99}Na_{0.01}Se$ as a representative) exhibit a lamellar microstructure (Figure 2a), which is consistent with the layered crystal structure. Large "domains"
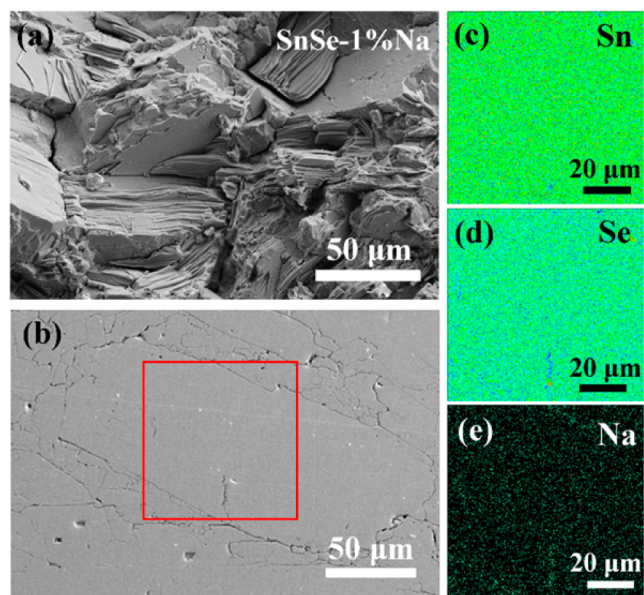

Figure 2. (a) Fractured and (b) polished surface morphologies, and EPMA mapping of (c) Sn, (d) Se, and (e) Na of $Sn_{0.99}Na_{0.01}Se$ as a representative. Results of more samples in backscattered electron (BSE) mode and elemental distribution by EDS can be found in Figures S1−S3 in the Supporting Information.

on the order of tens of micrometers were observed which contain many thin layers of the same orientation. Elements of Sn, Se, and Na (K) were found to have a homogeneous distribution down to the scale of 100 nm (Figure 2c−e, and Figures S1−S3). Structural analysis on nanoscale by TEM shows that the sample exhibits a layered structure (Figure 3a)
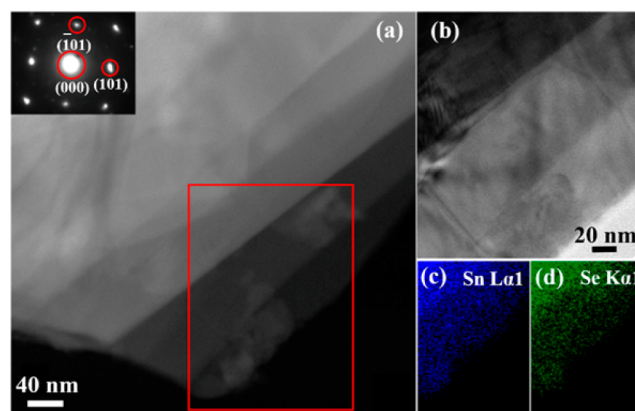

Figure 3. S/TEM and EDS analysis for $Sn_{0.99}Na_{0.01}Se$. (a) A high-angle annular dark-field (HAADF) image reveals the layered structure of the material. Bright and dark contrast represents the thickness difference of the specimen. The inset figure on the upper left corner is the corresponding selected area electron diffraction pattern along [010] direction. (b) A high-magnification TEM image shows the layered structure. (c,d) Elemental maps of Sn and Se from the rectangular region indicated in (a), showing elemental homogeneity of the specimen.

composed of crystalline lamellar grains (Figure 3b). The selected area electron diffraction pattern in Figure 3a was indexed as SnSe with a *Pnma* symmetry. Since the contrast in Figure 3a,b is a result of thickness variations, we can conclude that a homogeneity in lattice structure and distribution of Sn and Se was observed without nanoscale precipitates in the specimen.

Transport Properties and Doping Efficiency. Electrical transport properties of pristine and doped SnSe as a function of temperature are shown in Figure 4, which were measured perpendicular to the pressing direction of SPS. In general, undoped SnSe exhibits a large electrical resistivity (ρ) and Seebeck coefficient (S) at room temperature (RT). Upon doping with 1 at% of alkali elements, ρ is reduced markedly from 1.2 Ω·cm to 0.18, 0.036, and 0.011 Ω·cm along with a decrease of S from 480 μV/K to 359, 241, and 142 μV/K for Li-, K-, and Na-doping, respectively. Na-doping yields the lowest ρ and S, suggesting the highest carrier concentration. The temperature dependence of ρ and S is also changed by doping; pristine SnSe exhibits a semiconducting, thermally activated transport behavior, and becomes degenerate by 1% Na- and K-doping or ∼1.5% Li-doping (Figure S4). It is worth mentioning that in Na- and K-doped samples, ρ decreases from RT to ∼400 K, indicative of additional carrier scattering processes.[34] This type of variation was also found in several degenerate SnSe polycrystalline samples both in this work (Figures S4 and S5) and in some previous reports (dashed lines in Figure 4a),[18,20,22,35] and will be discussed in detail later. A high power factor (PF) of about 550 μW/mK^2 was obtained in the Na-doped sample at ∼800 K, which is 20−30% higher than for pristine SnSe and previously reported values.[20,22] As is known, thermal stability and property reversibility are
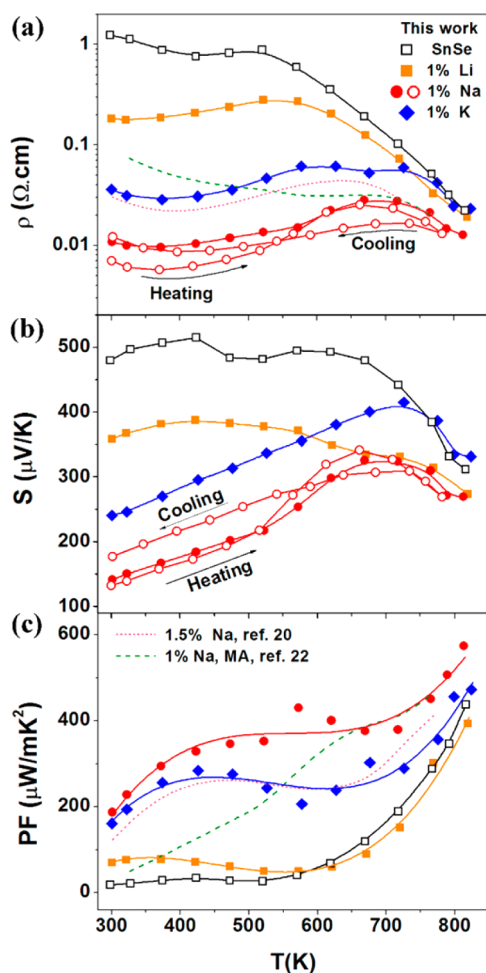
Figure 4. Electrical properties as a function of temperature for pristine and p-type doped SnSe. Data of another Na-doped sample in a heating and cooling cycle are given as red circles. Data from refs 20 and 22 are included for comparison.
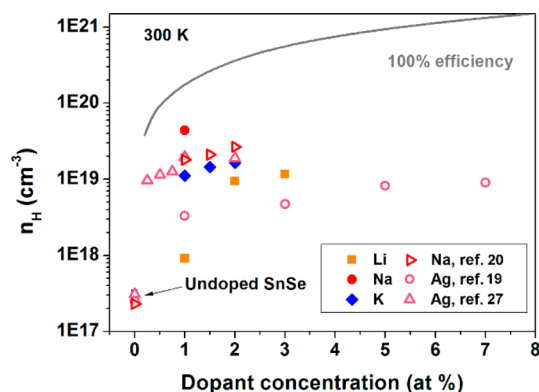

Figure 5. Measured Hall carrier concentration as a function of nominal concentration of dopants along with data from refs 19, 20, and 27. The line represents 100% doping efficiency.

important concerns for application of thermoelectric materials. In this work, electrical properties of another 1% Na-doped sample were tested in both heating and cooling processes. As shown in Figure 4a,b, the reversibility is acceptable despite a small hysteresis that was also found in Ag-doped polycrystalline SnSe.[19]

Interestingly, Na-doping is distinctly superior to K- or Li-doping in optimizing electrical properties. As shown in Figure 5, Na was found to give the best doping efficiency, yielding n_H = 4.4 × 10^{19} cm^{-3} at a doping amount of 1 at%. For 1% Li- and K-doped SnSe, n_H are only 9.0 × 10^{17} and 1.1 × 10^{19} cm^{-3} at RT, respectively, and saturate at ~1 × 10^{19} and ~2 × 10^{19} cm^{-3}, respectively. Here the carrier concentration for different dopants agrees well with the results from the optical absorption spectra (Figure 1d). It is also noted that for all dopants used here, the doping efficiency is far below the theoretical predications (gray line in Figure 5, assuming 100% doping efficiency).

Typically, doping efficiency is mainly limited by three factors: (1) the actual amount of dopants that enter the matrix, (2) the degree to which the doping atoms occupy Sn site, and (3) the amount of $M_{Sn}' + h^\bullet$ defect−hole pair (M = Li, Na, or K) and the number of holes that become free carriers.

For the first factor, possible loss of these alkali metals during synthesis and fabrication should not be ignored considering their high chemical activity. In fact, the actual content of Na (in 1% Na-doped sample) detected by ICP is quite close to the nominal one, while the amount of K is lower (see Table S1 in the Supporting Information). Nonetheless, even with the least loss, the carrier concentration of Na-doped sample is still significantly lower than the ideal estimation. These findings imply that in addition to the apparent composition, the following factors also matter. For the second factor, the existence of a second phase and nanoprecipitates (in 1% Na-doped sample) has been excluded, as shown in Figures 1−3. However, this does not mean that all the alkali atoms entering the matrix go to the "right" site. Actual occupancy (i.e., substitutional, interstitial, or intercalated type) of these dopants is an important concern. The third factor is an intrinsic property that is related to the formation energy of $M_{Sn}' + h^\bullet$ and the actual position of Fermi level after doping. Further clarification especially for the latter two factors is needed based on both experimental observation and theoretical calculation. Here, intuitively, we noticed that Na possesses moderate character: neither the lightest or smallest (Li) to easily move around, nor the most reactive with lowest boiling point (K) to evaporate, and thus is likely to be the best dopant among the three alkali metals.

To further understand the electrical properties and the underlying transport mechanisms in p-type doped SnSe polycrystals, high-temperature Hall measurements were carried out. As shown in Figure 6a, for undoped SnSe, n_H increases slightly from 3 × 10^{17} to 4 × 10^{17} cm^{-3} in the range of 300−523 K, and then rises exponentially, indicating thermal excitation of minority carriers (bipolar conduction). For Na- and K-doped samples, n_H is on the order of 10^{19} cm^{-3} at RT. It keeps nearly constant until ~550 K, and then decreases probably due to the transfer of carriers to the secondary and even lower sub-bands.[36]

The temperature dependence of mobility is rather complicated as shown in Figure 6b. For both pristine and doped samples in this work, μ_H increases with T from RT to ~400 K, and then decreases. The rapid rise of mobility at low temperatures is an indication of a barrier-like scattering that probably originates from oxidation, defects or impurities at grain boundaries.[37] This type of scattering mechanism was more clearly demonstrated in the fine-grained SnSe polycrystals synthesized by mechanical alloying (MA)[22] as shown in Figure
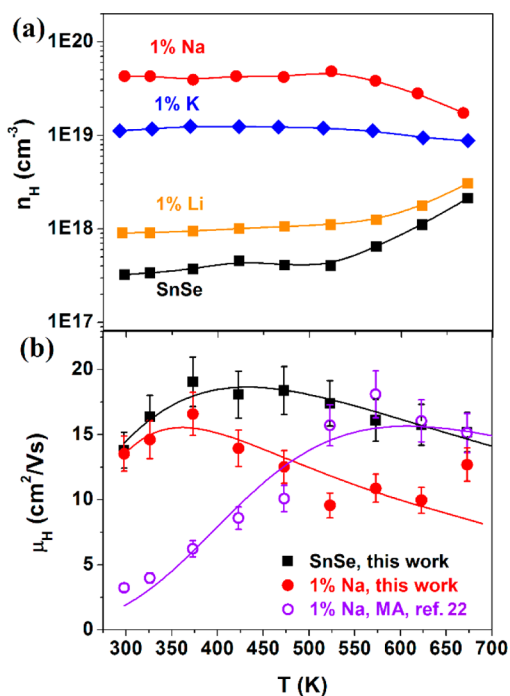
Figure 6. (a) Hall carrier concentration and (b) mobility varying with temperature for polycrystalline samples of SnSe. In (b), data of a Na-doped sample prepared by mechanical alloying (MA) was included.[22] Error bars represent 10% measurement uncertainty. Solid lines in (b) are calculated results considering a mixed scattering of carriers by acoustic phonons and grain boundaries.
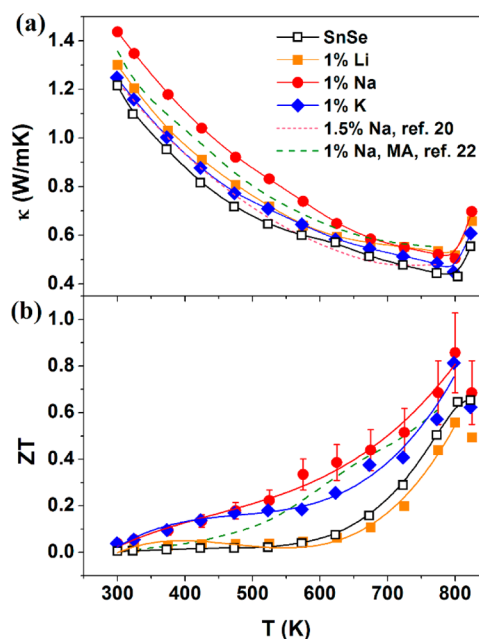

Figure 7. Temperature-dependent (a) thermal conductivity and (b) ZT for pristine and doped SnSe polycrystalline samples along with the data from refs 20 and 22. Error bars in (b) represent 20% uncertainty in ZT.

6b. Here to numerically explain the trend of mobility varying with temperature, we resorted to a mixed scattering process of carriers by acoustic phonons and grain boundaries.

In the case where various scattering mechanisms coexist, the mobility is related to the components determined by each scattering process:

$$\mu^{-1} = \mu_b^{-1} + \mu_{ac}^{-1} \tag{1}$$

The mobility limited by the grain-boundary scattering can be written as[37,38]

$$\mu_b(T) = A T^{-1/2} e^{-B/T} \tag{2}$$

where A and B are parameters that have a positive correlation to crystalline size and barrier height, respectively. Mobility determined by acoustic phonon scattering is considered proportional to $T^{-3/2}$:

$$\mu_{ac}(T) = C(T/300)^{-3/2} \tag{3}$$

with C being the RT mobility in the case where carriers are exclusively scattered by acoustic phonons.[3] The calculated results are shown as the solid curves in Figure 6b, in a good agreement with the experimental data. Furthermore, the barrier height ($E_B = Bk_B$) derived from eq 2 for the Na-doped sample synthesized by melting in this work (~118 meV) is lower than that of the MA-ed one (~179 meV). This is why the former exhibits a higher mobility at RT and a weaker increasing tendency with T than the latter.

As shown in Figure 7a, the thermal conductivity decreases with increasing temperature until ~800 K, implying dominant phonon–phonon interaction, and sharply rises at higher temperatures probably due to the known $Pnma-Cmcm$ phase transition[14] as well as bipolar excitation.[39,40] Undoped SnSe exhibits a slightly lower thermal conductivity than doped ones due to a smaller contribution from carriers. Benefiting from the high carrier concentration and electrical conductivity, a maximum $ZT = 0.85$ was achieved in 1% Na-doped sample at 800 K, being ~30% higher than those of undoped samples and the mechanically alloyed Na-doped sample[22] (see Figure 7b). Relatively high $ZT = 0.80$ was also obtained in K-doped samples.

Band Structure and Mobility. As has been shown by electronic band calculation, the existence of multiple valleys in the valence band is key to the large Seebeck coefficient in heavily doped p-type SnSe.[15,16] It is also noticed that the band offset between the first valence band maxima (VBM1) and the second one (VBM2) is only 0.02–0.06 eV,[15] being less than $3k_BT$ at room temperature. This offset is so small that the two bands may be considered degenerate. In addition, it is known that the single parabolic band (SPB) model is a rough yet insightful tool to understand the band structure and scattering process of semiconductors.[41] Here we calculated the Pisarenko plot (Seebeck coefficient vs carrier concentration) using both SPB and two-band models, and compared the fitting results with the experimental data from this and previous studies over a wide range of carrier concentration. Calculation details are given in section 3 of the Supporting Information.

On the one hand, if we consider the two bands as an equivalent, single band, the combined density-of-state effective mass can be derived from the two components:[40,42]

$$m_d^{*3/2} = m_{d,1}^{*3/2} + m_{d,2}^{*3/2} \tag{4}$$

yielding $m_d^* = 0.97\ m_0$ (m_0 is the free electron mass). By further assuming that carriers are dominantly scattered by acoustic phonons, a satisfactory fitting was obtained as demonstrated by the gray, solid line in Figure 8. It was also found that $m_d^* = 1.1\ m_0$ is the best fitting value (dashed line), and is quite close to the above one directly derived from the two sub-bands.
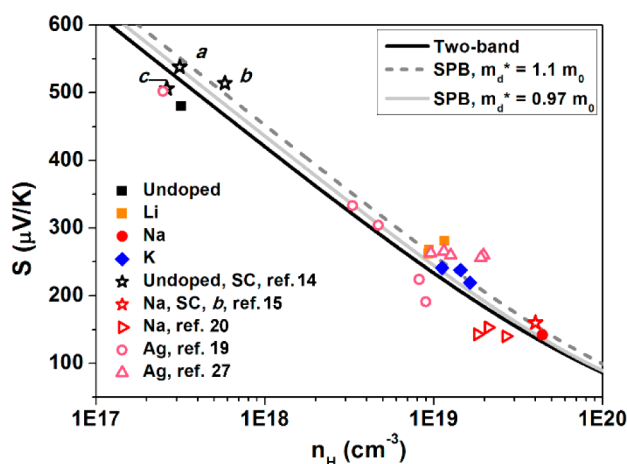
Figure 8. Seebeck coefficient as a function of Hall carrier concentration at room temperature. Solid dots are experimental data in this work, while open dots are from refs 14, 15, 19, 20, and 27 for both polycrystals and single crystals (SC). All the data for polycrystalline samples are in-plane measurements. The black solid line was calculated using two-band model, while the gray solid and gray dashed lines were derived from the single parabolic band (SPB) model with the effective masses of 0.97 and 1.1 m_0, respectively.

Figure 9. Hall mobility as a function of Hall carrier concentration for undoped and heavily doped SnSe at room temperature. Data from refs 14, 15, 19, and 27 are included. The two lines were calculated using SPB by adjusting μ_0 (Supporting Information, eq S7), and the curved arrows were added to guide the eyes. All the data of polycrystalline samples refer to in-plane measurements.

On the other hand, the calculation using the two-band model[43−45] was also carried out where the sub-bands were treated as parabolic and their band offset was taken as 0.02 eV.[15] The fitting result is depicted as the black line in Figure 8, and is roughly consistent with SPB. It is also seen that the two-band model gives a slightly lower Seebeck coefficient than SPB at low doping levels, yet yielding nearly the same values at higher carrier concentration; that is, the loss of Seebeck coefficient from low to high doping level is smaller in a two-band system than its "equivalent" single band system, which is owing to the existence of the heavier secondary band.[8,43,46] Although allowance for adjustment of parameters will give even better results, as a preliminary and concise model, a modified SPB here is adequate to capture the varying tendency of S with n_H at least within the limit of 4.4×10^{19} cm^{-3} due to the small band offset. At even higher doping levels, even lower sub-bands will possibly start making a difference.[16]

Although n_H and S can be tuned close to that of single crystals, μ_H of polycrystals from this and previous reports is significantly lower. As shown in Figure 9, μ_H in single crystals along b-axis is 5−10 times as large as that of polycrystals in both undoped and doped cases. In addition, μ_H of polycrystals decreases more rapidly with n_H than the trend predicted by SPB, especially for Li- and K-doping cases, while Na- and Ag-doped samples show an intermediate tendency.

The low mobility in SnSe polycrystals over the entire range of carrier concentration reflects the polycrystalline nature of the samples which contain misoriented crystallites. In single crystals, carriers along b-axis have the highest mobility while holes along a-axis show the lowest one.[14] If the orientation of crystallites is random, the mobility can be expected to be an averaged value of that of the single crystals. It has been shown that $\mu_H = 100$ cm^2/(V·s) is a reasonable estimation for the nondegenerate limit at RT,[47] which is only one-third to one-half of $\mu_{H,b\text{-axis}}$. Further decrease of mobility is probably caused by the grain-boundary scattering as well as other scattering processes due to samples' imperfect quality. In addition, dopants or impurity atoms tend to disturb the pseudopotential
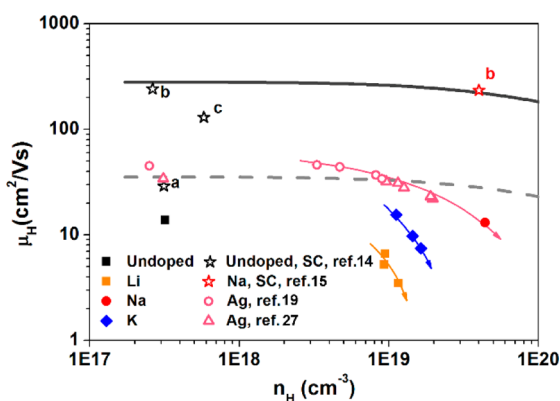
of the lattice, acting as scattering centers of carriers.[34,36] A larger difference in atomic size between dopants and the matrix will result in a stronger potential-based interaction and carrier scattering. Here we notice that the effective radii of Ag$^+$ and Na$^+$ are 1.15 and 1.02 Å, respectively,[48] which are close to that of Sn^{2+} (1.12 Å),[49] while the values for Li$^+$ and K$^+$ are 0.76 and 1.38 Å, respectively.[48] This is likely to be the one of the reasons why μ_H of Li- and K-doped samples decrease more sharply with n_H than Na- and Ag-doped ones.

Considering the fact that the total thermal conductivity of SnSe polycrystals is no larger than that of Na-doped single crystals (b-axis, ref 15), the low mobility is thus the bottleneck for improving thermoelectric performance of polycrystalline SnSe, especially at low temperatures. Efforts then should be devoted to preventing the mobility from being severely impaired. First, strong microstructure anisotropy resembling the single-crystal character should be recreated in polycrystals. In fact, texture modulation[23,24] has been revealed as an effective method to improve the performance of polycrystalline SnSe while long-time milling or grinding[22] is not recommended. Second, defects at grain boundaries should be controlled or decorated[50] to suppress carrier scattering. Finally, dopants should be judiciously selected and their amount should be carefully controlled.

■ CONCLUDING REMARKS

In summary, the effect of Li-, Na-, and K-doping on thermoelectric properties of SnSe polycrystals was comparatively studied. All alkali dopants enhanced the carrier concentration and electrical conductivity of SnSe. Na was found to have the best doping efficiency, increasing the Hall carrier concentration to 4.4×10^{19} cm^{-3} at 300 K while maintaining a relatively large Seebeck coefficient of 142 μV/K. Due to the small offset between the first two valence bands, a modified, equivalent SPB model is adequate to understand the dependence of Seebeck coefficient on doping level within 4.4×10^{19} cm^{-3}. The temperature dependence of mobility was quantitatively described using a synergetic mechanism combining acoustic phonon scattering and grain-boundary scattering. A maximum ZT of ~0.8 was achieved in 1% Na- and K-doped samples, being 30% higher than pristine SnSe. The findings and analyses in this study will be helpful to understand thermo-

electric transport properties of SnSe and to further optimize the thermoelectric performance in polycrystalline specimens.

■ ASSOCIATED CONTENT

Ⓢ Supporting Information

The Supporting Information is available free of charge on the ACS Publications website at DOI: 10.1021/jacs.6b04181.

> Elemental distribution and composition (Figures S1−S3 and Table S1); thermoelectric properties of Li- and K-doped samples (Figures S4 and S5); calculation details using SPB and two-band models with related parameters (Table S2 and Figure S6) (PDF)

■ AUTHOR INFORMATION

Corresponding Author

*jingfeng@mail.tsinghua.edu.cn

Author Contributions

‖T.-R.W. and G.T. contributed equally to this work.

Notes

The authors declare no competing financial interest.

■ ACKNOWLEDGMENTS

■ REFERENCES

(1) Bell, L. E. *Science* **2008**, *321*, 1457.

(2) Snyder, G. J.; Toberer, E. S. *Nat. Mater.* **2008**, *7*, 105.

(3) Nolas, G. S.; Sharp, J.; Goldsmid, H. J. *Thermoelectrics: Basic Principles and New Materials Developments*; Springer: Berlin, 2001.

(4) Kanatzidis, M. G. *Chem. Mater.* **2010**, *22*, 648.

(5) Yang, J.; Yip, H.-L.; Jen, A. K.-Y. *Adv. Energy Mater.* **2013**, *3*, 549.

(6) Biswas, K.; He, J.; Blum, I. D.; Wu, C.-I; Hogan, T. P.; Seidman, D. N.; Dravid, V. P.; Kanatzidis, M. G. *Nature* **2012**, *489*, 414.

(7) Wang, H.; Gibbs, Z. M.; Takagiwa, Y.; Snyder, G. J. *Energy Environ. Sci.* **2014**, *7*, 804.

(8) Pei, Y.; Shi, X.; LaLonde, A.; Wang, H.; Chen, L.; Snyder, G. J. *Nature* **2011**, *473*, 66.

(9) Kim, S. I.; Lee, K. H.; Mun, H. A.; Kim, H. S.; Hwang, S. W.; Roh, J. W.; Yang, D. J.; Shin, W. H.; Li, X. S.; Lee, Y. H.; Snyder, G. J.; Kim, S. W. *Science* **2015**, *348*, 109.

(10) Hu, L.; Zhu, T.; Liu, X.; Zhao, X. *Adv. Funct. Mater.* **2014**, *24*, 5211.

(11) Liu, H.; Shi, X.; Xu, F.; Zhang, L.; Zhang, W.; Chen, L.; Li, Q.; Uher, C.; Day, T.; Snyder, G. J. *Nat. Mater.* **2012**, *11*, 422.

(12) Ying, P.; Liu, X.; Fu, C.; Yue, X.; Xie, H.; Zhao, X.; Zhang, W.; Zhu, T. *Chem. Mater.* **2015**, *27*, 909.

(13) Lu, X.; Morelli, D. T.; Xia, Y.; Zhou, F.; Ozolins, V.; Chi, H.; Zhou, X.; Uher, C. *Adv. Energy Mater.* **2013**, *3*, 342.

(14) Zhao, L.-D.; Lo, S.-H.; Zhang, Y.; Sun, H.; Tan, G.; Uher, C.; Wolverton, C.; David, V. P.; Kanatzidis, M. G. *Nature* **2014**, *508*, 373.

(15) Zhao, L.-D.; Tan, G.; Hao, S.; He, J.; Pei, Y.; Chi, H.; Wang, H.; Gong, S.; Xu, H.; Dravid, V. P.; Uher, C.; Snyder, G. J.; Wolverton, C.; Kanatzidis, M. G. *Science* **2016**, *351*, 141.

(16) Peng, K.; Lu, X.; Zhan, H.; Hui, S.; Tang, X.; Wang, G.; Dai, J.; Uher, C.; Wang, G.; Zhou, X. *Energy Environ. Sci.* **2016**, *9*, 454.

(17) Li, C. W.; Hong, J.; May, A. F.; Bansal, D.; Chi, S.; Hong, T.; Ehlers, G.; Delaire, O. *Nat. Phys.* **2015**, *11*, 1063.

(18) Zhang, Q.; Chere, E. K.; Sun, J.; Cao, F.; Dahal, K.; Chen, S.; Chen, G.; Ren, Z. *Adv. Energy Mater.* **2015**, *5*, 1500360.

(19) Chen, C.-L.; Wang, H.; Chen, Y.-Y.; Day, T.; Snyder, G. J. *J. Mater. Chem. A* **2014**, *2*, 11171.

(20) Chere, E. K.; Zhang, Q.; Dahal, K.; Cao, F.; Mao, J.; Ren, Z. *J. Mater. Chem. A* **2016**, *4*, 1848.

(21) Han, Y.-M.; Zhao, J.; Zhou, M.; Jiang, X.-X.; Leng, H.-Q.; Li, L.-F. *J. Mater. Chem. A* **2015**, *3*, 4555.

(22) Wei, T.-R.; Wu, C.-F.; Zhang, X.; Tan, Q.; Sun, L.; Pan, Y.; Li, J.-F. *Phys. Chem. Chem. Phys.* **2015**, *17*, 30102.

(23) Fu, Y.; Xu, J.; Liu, G.-Q.; Yang, J.; Tan, X.; Liu, Z.; Qin, H.; Shao, H.; Jiang, H.; Liang, B.; Jiang, J. *J. Mater. Chem. C* **2016**, *4*, 1201.

(24) Popuri, S. R.; Pollet, M.; Decourt, R.; Morrison, F. D.; Bennett, N. S.; Bos, J. W. G. *J. Mater. Chem. C* **2016**, *4*, 1685.

(25) Zhang, Q.; Cao, F.; Liu, W.; Lukas, K.; Yu, B.; Chen, S.; Opeil, C.; Broido, D.; Chen, G.; Ren, Z. *J. Am. Chem. Soc.* **2012**, *134*, 10031.

(26) He, J.; Zhao, L.-D.; Zheng, J.-C.; Doak, J. W.; Wu, H.; Wang, H.-Q.; Lee, Y.; Wolverton, C.; Kanatzidis, M. G.; Dravid, V. P. *J. Am. Chem. Soc.* **2013**, *135*, 4624.

(27) Leng, H.; Zhou, M.; Zhao, J.; Han, Y.; Li, L. *J. Electron. Mater.* **2016**, *45*, 527.

(28) Leng, H.-Q.; Zhou, M.; Zhao, J.; Han, Y.-M.; Li, L.-F. *RSC Adv.* **2016**, *6*, 9112.

(29) Wang, X.; Xu, J.; Liu, G.; Fu, Y.; Liu, Z.; Tan, X.; Shao, H.; Jiang, H.; Tan, T.; Jiang, J. *Appl. Phys. Lett.* **2016**, *108*, 083902.

(30) Burstein, E. *Phys. Rev.* **1954**, *93*, 632.

(31) Kaiser, W.; Fan, H. Y. *Phys. Rev.* **1955**, *98*, 966.

(32) Yu, P. Y.; Cardona, M. *Fundamentals of Semiconductors*; Springer: Berlin, 2010.

(33) Schroder, D. K.; Thomas, R. N.; Swartz, J. C. *IEEE J. Solid-State Circuits* **1978**, *13*, 180.

(34) Ziman, J. M. *Electrons and Phonons: The Theory of Transport Phenomena in Solids*; Oxford University Press: New York, 1960.

(35) Sassi, S.; Candolfi, C.; Vaney, J.-B.; Ohorodniichuk, V.; Masschelein, P.; Dauscher, A.; Lenoir, B. *Appl. Phys. Lett.* **2014**, *104*, 212105.

(36) Ravich, Y. I.; Efimova, B. A.; Smirnov, I. A. *Semiconducting Lead Chalcogenides*; Springer Science & Business Media: New York, 1970.

(37) Seto, J. Y. W. *J. Appl. Phys.* **1975**, *46*, 5247.

(38) Martin, J.; Wang, L.; Chen, L.; Nolas, G. S. *Phys. Rev. B: Condens. Matter Mater. Phys.* **2009**, *79*, 115311.

(39) Price, P. J. *Philos. Mag.* **1955**, *46*, 1252.

(40) Rowe, D. M. *CRC Handbook of Thermoelectrics*; CRC Press: Boca Raton, FL, 1995.

(41) May, A. F.; Snyder, G. J. In *Thermoelectrics and Its Energy Harvesting*; Rowe, D. M., Ed.; CRC Press: Boca Raton, FL, 2012; Chap. 11.

(42) Heremans, J. P.; Jovovic, V.; Toberer, E. S.; Saramat, A.; Kurosaki, K.; Charoenphakdee, A.; Yamanaka, S.; Snyder, G. J. *Science* **2008**, *321*, 554.

(43) Tang, Y.; Gibbs, Z. M.; Agapito, L. A.; Li, G.; Kim, H.-S.; Nardelli, M. B.; Curtarolo, S.; Snyder, G. J. *Nat. Mater.* **2015**, *14*, 1223.

(44) Chasapis, T. C.; Lee, Y.; Hatzikraniotis, E.; Paraskevopoulos, K. M.; Chi, H.; Uher, C.; Kanatzidis, M. G. *Phys. Rev. B: Condens. Matter Mater. Phys.* **2015**, *91*, 085207.

(45) Putley, E. H. *J. Phys. C: Solid State Phys.* **1975**, *8*, 1837.

(46) Tan, G.; Shi, F.; Hao, S.; Chi, H.; Bailey, T. P.; Zhao, L.-D.; Uher, C.; Wolverton, C.; Dravid, V. P.; Kanatzidis, M. G. *J. Am. Chem. Soc.* **2015**, *137*, 11507.

(47) Guo, R.; Wang, X.; Kuang, Y.; Huang, B. *Phys. Rev. B: Condens. Matter Mater. Phys.* **2015**, *92*, 115202.

(48) Shannon, R. D. *Acta Crystallogr., Sect. A: Cryst. Phys., Diffr., Theor. Gen. Crystallogr.* **1976**, *32*, 751.

(49) Tan, Q.; Zhao, L.-D.; Li, J.-F.; Wu, C.-F.; Wei, T.-R.; Xing, Z.-B.; Kanatzidis, M. G. *J. Mater. Chem. A* **2014**, *2*, 17302.

(50) Tan, G.; Chi, H.; Liu, W.; Zheng, Y.; Tang, X.; He, J.; Uher, C. *J. Mater. Chem. C* **2015**, *3*, 8372.